Article ID: 1006-8775(2017) 03-0259-10

A MODELING STUDY OF PARAMETERIZATION SCHEMES FOR DEPOSITIONAL GROWTH OF ICE CRYSTAL: FOUR RAINFALL CASES OVER TROPICS AND MIDLATITUDES

XIN Jin (辛 进)[1], LI Xiao-fan (李小凡)[1]
(School of Earth Sciences, Zhejiang University, Hangzhou 310027 China)

Abstract: Depositional growth of ice crystal is one of the major processes for development of precipitation systems and can be represented by depositional growth of cloud ice from cloud water (P_{IDW}) and depositional growth of snow from cloud ice (P_{SFI}) in cloud-resolving model. Four parameterization schemes are analyzed in the cloud-resolving model simulations of four rainfall cases over the tropics and midlatitudes. The comparison of time and model domain mean data shows that Shen's scheme produces the closest rainfall simulation to the observation. Compared to Zeng's scheme, Shen's scheme improves the mean rain-rate simulation significantly through the dramatic decrease in depositional growth of cloud ice from cloud water. Compared to other schemes, Shen's scheme produces the better rainfall simulation via the reduction in the mean rain rate associated with the enhanced gain of cloud water and ice.

Key words: depositional growth of ice crystal; rainfall simulation; rain rate; cloud-resolving-model simulation
CLC number: P456.7 **Document code:** A
doi: 10.16555/j.1006-8775.2017.03.003

1 INTRODUCTION

Ice clouds are an important ingredient of precipitation systems since the melting of precipitation ice is one of the major rainfall sources. Ice clouds can also affect heat balance through the release of latent heat during the formation of ice hydrometeor and the change in radiation due to the prevention of solar radiation from reaching the earth surface and the reduction of infrared radiation going out to the space. Thus, the accurate numerical modeling of clouds and precipitation relies on the improvement of the presentation of ice clouds and associated ice microphysical processes. Among various ice microphysical processes, the depositional growth of ice crystal is one of most important processes for the development of ice clouds and can be presented by depositional growth of cloud ice from cloud water (P_{IDW}) and depositional growth of snow from cloud ice (P_{SFI}) in cloud-resolving models.

Hsie et al.[1] used a natural ice nucleus mass and the artificial ice crystal (the sizes from 40 to 50 μm in radius) in the calculations of P_{IDW} and P_{SFI}, respectively, which produce a small amount of cloud ice. Based on the analysis of in-situ aircraft observations, the mean effective sizes of ice crystal ranged from 24 to 124 μm in radius (Fu and Liou [2]). Therefore, Krueger et al.[3] increased the size of ice crystal (from 40 to 100 μm in radius) in the calculation of P_{SFI}, which was more realistic as well as could be observed by optical probe, and replaced a natural ice nucleus mass with an averaged mass of ice crystal in the calculation of P_{IDW}, which cause a significant increase in cloud ice and a moderate increase in snow (e.g., Li et al.[4]). Zeng et al.[5] proposed a linear relation between the number and mass of ice crystal in the small range of ice crystal radius (0–50 μm) to develop new schemes for P_{SFI} and P_{IDW} and revealed significant enhancement in cloud ice. The scheme is used to study the contribution by ice nuclei to global warming (Zeng et al.[6]) and the indirect effect of ice nuclei on atmospheric radiation (Zeng et al.[7]). Shen et al. [8] modified Zeng's scheme through the replacement of ice crystal radius from 0–50 μm to 40–50 μm (the low limit of 40 μm referred to Hsie et al.[1], Lin et al. [9], Krueger et al. [3]), which suppresses the development of cloud ice.

The objective of this study is to test parameterization schemes for better rainfall simulation through the comparison between simulated rain rates and rain gauge observations and to give the physical explanations via the analysis of cloud microphysical and heat budgets. Four rainfall cases are chosen from tropics to midlatitudes. In the next section, model, parameterization schemes and design of experiments are described. The results are presented in section 3. A summary is given in section 4.

Received 2016-03-09; **Revised** 2017-05-16; **Accepted** 2017-08-15
Foundation item: National Natural Science Foundation of China (41475039), National Key Basic Research and Development Project of China (2015CB953601)
Biography: LI Xiao-fan, Ph. D., Professor, primarily undertaking research on mesoscale meteorology, cloud microphysics.
Corresponding author: LI Xiao-fan, e-mail: xiaofanli@zju.edu.cn

2 MODEL AND EXPERIMENTS

The model used here is the two-dimensional version of Goddard Cumulus Ensemble Model. The model was originally developed by Soong and Ogura[10], Soong and Tao[11] and Tao and Simpson[12] and modified by Sui et al.[13-14] and Li et al.[4]. The periodic boundary conditions are furnished in the model. The perturbation zonal wind and vertical velocity are predicted during the model integration. The model also includes prognostic equations for specific humidity with cloud microphysical parameterization schemes from Hsie et al.[1], Lin et al.[9], Rutledge and Hobbs [15-16], Tao et al.[17], Krueger et al.[3], Zeng et al.[5] and Shen et al.[8] and for potential temperature with the radiative parameterization schemes from Chou et al.[18-19] and Chou and Suarez[20] and the release of latent heat calculated from cloud microphysical parameterization schemes. The basic parameters are model domain of 768 km, horizontal grid of 1.5 km, time step of 12 s and 33 vertical levels. The two-dimensional framework is used in this study because of similarities in two- and three-dimensional model simulations in terms of thermodynamics, surface heat fluxes, rainfall, precipitation efficiency, and vertical transports of mass, sensible heat, and moisture (e.g., Tao and Soong [21]; Tao et al.[22]; Grabowski et al.[23]; Tompkins[24]; Khairoutdinov and Randall[25]; Sui et al.[26].

The tropical rainfall case during Tropical Ocean Global Atmosphere-Coupled Ocean Atmosphere Response Experiment (TOGA COARE) (Li et al.[4]), pre-summer torrential rainfall case during June 2008 (Wang et al.[27]; Shen et al.[28]), Meiyu heavy rainfall case during June 2011 (Zhai et al.[29]), and Harbin torrential rainfall case in July 2012 are selected in this study and their experiments are denoted by TOGA, PSR, MYR, and HBR, respectively. The domains for calculating large-scale forcing are Intensive Flux Array centered at 156 °E, 2 °S for TOGA, 108–116 °E, 21–22 °N for PSR, 114–122 °E, 29–31 °N for MYR and 122–130 °E, 45–48 °N for HBR. The model simulation integration periods are 1000 LST 19 December-1000 LST 24 December 1992 (5 days) for TOGA, 0200 LST 3 June–0200 LST 8 June 2008 (5 days) for PSR, 0800 LST 9 June–0800 LST 20 June 2011 (11 days) for MYR and 0800 LST 28 July–0800 LST 31 July 2012 (3 days) for HBR. The vertical velocity and zonal wind are derived by Sui et al.[14] based on the TOGA COARE observations within the Intensive Flux Array (IFA) region in TOGA case and are obtained by the Global Data Assimilation System (GDAS) developed by the National Centers for Environmental Prediction (NCEP), National Oceanic and Atmospheric Administration (NOAA), USA in PSR case (Shen et al.[28]), by NCEP reanalysis R2 in MYR case (Zhai et al.[29]) and NCEP Final (FNL) Operational Global analysis data in HBR case. Vertical profiles of time-mean vertical velocity and zonal wind imposed in the model show prevailed upward motions through the troposphere with maximum upward motions around 8.5 km (Fig.1a). The upward motions are strongest in PSR, while they are weakest in TOGA. Westerly winds increases from the surface to 3 km and then decreases from 3 km to 12 km in TOGA (Fig. 1b). PSR also shows similar increase in westerly wind below 3 km, but westerly winds do not change much above 3 km in PSR. Westerly winds increase through the troposphere linearly in MYR. Easterly winds appear near the surface and switch to westerly wind around 2km and then the westerly winds increase from 2 km to 12 km linearly in HBR.

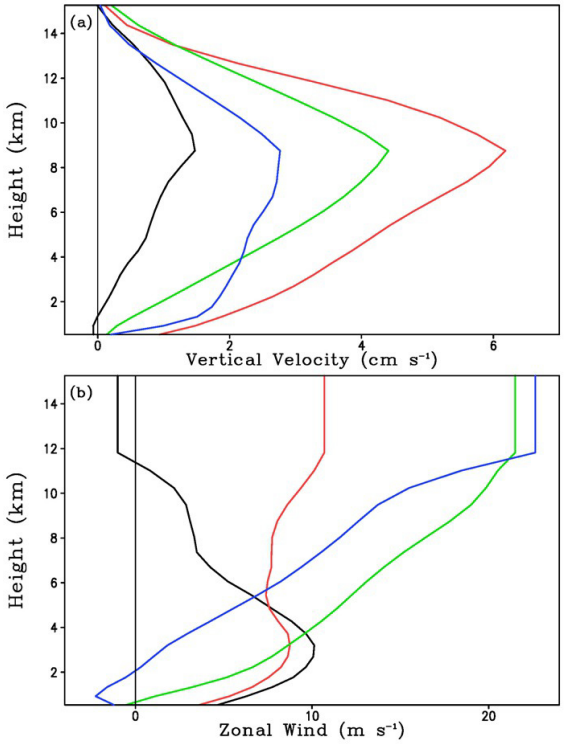

Figure 1. Vertical profiles of time-mean (a) vertical velocity (cm s^{-1}) and (b) zonal wind (m s^{-1}) imposed in the model in TOGA (black), PSR (red), MYR (green) and HBR (blue).

The observed rain-rate data in TOGA case are obtained by the Tropical Rainfall Measuring Mission office at NASA/Goddard Space Flight Center and is based on radar reflectivity data taken from the Massachusetts Institute of Technology Doppler radar and the TOGA radar, which are located within the IFA region (Short et al.[30]), which are averaged over a 150× 150 km^2 area (Li et al.[4]). The observed rain rates in PSR case are from rain-gauge data averaged from 17 stations over southern Guangdong and Guangxi (Shen et al.[28]). The observed rain rates in MYR and HBR cases are from the data merged by rain gauge data from automatic weather stations and NCEP Climate Precipitation Center (CPC) MORPHing technique (CMORPH) (Joyce et al.[31]).

The four schemes that parameterize P_{SFI} and P_{IDW} from Hsie et al.[1], Krueger et al.[3], Zeng et al.[5] and

Shen et al.[8] are used in the simulations of the four rainfall events (see the summary of these schemes in Table 1). The parameterization schemes of P_{SFI} and P_{IDW} used in the model simulations are Hsie et al.[1] for Hsie, Krueger et al.[3] for Krueger, Zeng et al.[5] for ZengL, ZengM and ZengH and Shen et al.[8] for Shen. Following Zeng et al.[32], the parameters β and n_o for the formulation of ice crystal concentration from Fletcher[33] are 0.4 and 10^{-9} cm^{-3} for ZengL, 0.5 and 5×10^{-9} cm^{-3} for ZengM and 0.55 and 10^{-7} cm^{-3} for ZengH. Thus, for each rainfall case, a set of 6 simulations (Hise, Krueger, ZengL, ZengM, ZengH and Shen) will be simulated and analyzed. We use the pre-summer rainfall simulation data (PSR_Hsie, PSR_Krueger, PSR_ZengL, PSR_ZengM, PSR_ZengH and PSR_Shen) from Shen et al.[8], the tropical rainfall simulation (TOGA_Krueger) from Li et al.[4] and the Meiyu rainfall simulation (MYR_Krueger) from Zhai et al.[29]. The other simulations are carried out in this study. Only time and model domain mean simulation data are analyzed in the following discussions. Time averages are taken in 5 days for the TOGA and PSR simulations, 11 days for the MYR simulations and 3 days for the HBR simulations respectively.

Table 1. Summary of schemes that parameterize the depositional growth of cloud ice from cloud water (P_{IDW}) and the depositional growth of snow from cloud ice (P_{SFI}).

Scheme	Description
Hsie et al.[1]	$P_{IDW}=\frac{n_0 e^{\frac{1}{2}\lvert T-T_o\rvert}}{10^3\rho}a_1(m_n)^{a_2}$, $P_{SFI}=\frac{q_i}{\Delta t_1}$, where $n_0=10^{-8}m^{-3}$; $T_0=0^oC$; m_n=$1.05\times10^{-15}g$; ρ is the air density, which only is a function of height; a_1 and a_2 are the positive temperature-dependent coefficients (Koenig 1971). q_i is the mixing ratio of cloud ice; $\Delta t_1[=(m_{I50}{}^{1-a_2}-m_{I40}{}^{1-a_2})/a_1(1-a_2)]$ is the timescale needed for a crystal to grow from radius r_{I40} to radius r_{I50}; $m_{I50}(=4.8\times10^{-10}kg)$ is the mass of an ice crystal r_{I50} (=50 μm), and $m_{I40}(=2.46\times10^{-10}kg)$ is the mass of an ice crystal r_{I40} (=40 μm).
Krueger et al.[3]	$P_{IDW}=\frac{n_0 e^{\frac{1}{2}\lvert T-T_o\rvert}}{10^3\rho}a_1(\frac{\rho q_i}{n_0 e^{\frac{1}{2}\lvert T-T_o\rvert}})^{a_2}$ $P_{SFI}=\frac{q_i}{\Delta t_1}$, where $\Delta t_1=(m_{I100}{}^{1-a_2}-m_{I40}{}^{1-a_2})/a_1(1-a_2)$, m_{I100} $(=3.84\times10^{-9}\mathrm{kg})$ is the mass of an ice crystal r_{I100} (=10^2 μm).
Zeng et al.[5]	$P_{IDW}=\frac{2}{(a_2+1)(a_2+2)}[3a_2q_i+(1-a_2)m_{I50}\mu\rho^{-1}N_i]a_1m_{I50}^{a_2-1}$, $P_{SFI}=\max[2a_1(3q_i-m_{I50}\mu\rho^{-1}N_i)m_{I50}^{a_2-1},0]$, where $N_i=n_0e^{\beta(T_0-T)}$, β varies from 0.4 to 0.6, and n_o varies from 10^{-9} cm^{-3} to 10^{-6} cm^{-3} (Fletcher 1962); μ(=1.2) is the ice particle enhancement factor due to a riming-splintering mechanism (Hallet and Mossop 1974).
Shen et al.[8]	$P_{IDW}=\frac{2}{(a_2+1)(a_2+2)}[3a_2f_1q_i+(1-a_2)f_2m_{I50}\mu\rho^{-1}N_i]a_1m_{I50}^{b_2-1}$, $P_{SFI}=2a_1(3f_1q_i-f_2m_{I50}\mu\rho^{-1}N_i)m_{I50}^{a_2-1}$, where $f_1=1-(\frac{1}{2})^{a_2-1}$, $f_2=1-(\frac{1}{2})^{a_2}$.

The mean mass-integrated cloud budget is expressed by

$$P_S = Q_{NC} + Q_{CM} \quad (1)$$

Here Q_{NC} is the net condensation and Q_{CM} is hydrometeor change.

Hydrometeor change (Q_{CM}) can be further broken down to the mean hydrometeor change in cloud water (Q_{CMW}), raindrops (Q_{CMR}), cloud ice (Q_{CMI}), snow (Q_{CMS}) and graupel (Q_{CMG}).

$$Q_{CM} = Q_{CMW} + Q_{CMR} + Q_{CMI} + Q_{CMS} + Q_{CMG} \quad (2)$$

Q_{CMW} and Q_{CMI} can be approximately written as

$$Q_{CMW}=P_{SACW}+P_{RAUT}+P_{RACW}+P_{GACW}+P_{IDW}-P_{CND}. \quad (3a)$$

$$Q_{CMI}=P_{SAUT}+P_{SACI}+P_{SFI}+P_{GACI}-P_{IDW}-P_{DEP}. \quad (3b)$$

P_{SACW} is growth of snow by the accretion of cloud water; P_{RAUT} is growth of raindrops by the autoconversion of cloud water; P_{RACW} is growth of raindrops by the collection of cloud water; P_{GACW} is growth of graupel by the accretion of cloud water; P_{CND} is growth of cloud water by condensation of supersaturated vapor; P_{SAUT} is growth of snow by the conversion of cloud ice; P_{SACI} is growth of snow by the collection of cloud ice; P_{GACI} is growth of graupel by the collection of cloud ice; P_{DEP} is growth of cloud ice by the deposition of supersaturated vapor.

3 RESULTS

In the four rainfall-case simulations with Hsie's scheme, P_{IDW} is negligibly small due to the use of a natural ice nucleus (Table 2). When the radius of ice crystal increases from 50 μm to 100 μm in Krueger's scheme, P_{SFI} decreases by 42.5%–51.3%, which leads to the increases in cloud ice (e.g., 0.16 mm in MYR_Hsie versus 0.71 mm in MYR_Krueger). This is consistent to the results from Li et al.[4]. P_{IDW} increases by the four orders of magnitudes. As Fletcher's parameters increase from ZengL to ZengH, P_{IDW} increases by several orders of magnitudes, while P_{SFI} barely changes. This causes a significant increase in cloud ice from ZengL to ZengH (e.g., 0.15 mm in MYR_ZengL versus 26.96 mm in MYR_ZengH). Compared with ZengH, Shen cuts 40%–60% of P_{SFI} and reduces P_{IDW} by three orders of magnitudes, which leads to a significant decrease in cloud ice (e.g., 26.96 mm in MYR_ZengH versus 7.72 mm in MYR_Shen).

Table 2. Time-mean mass-integrations of depositional growth of snow from cloud ice ($[P_{SFI}]$), the depositional growth of cloud ice from cloud water ($[P_{IDW}]$) and mixing ratio of cloud ice $[q_i]$ in the four sets of simulations. Units are mm d^{-1} for $[P_{SFI}]$ and $[P_{IDW}]$ and mm for $[q_i]$.

Scheme	$[P_{SFI}]$	$[P_{IDW}]$	$[q_i]$
TOGA_Hsie	2.36	$1.5\ 10^{-7}$	0.17
TOGA_Krueger	1.35	$1.2\ 10^{-3}$	0.88
TOGA_ZengL	3.40	$5.1\ 10^{-3}$	0.43
TOGA_ZengM	3.23	$1.7\ 10^{-2}$	1.57
TOGA_ZengH	2.98	3.65	32.53
TOGA_Shen	1.81	$2.6\ 10^{-3}$	7.87
PSR_Hsie	3.18	$3.0\ 10^{-7}$	0.23
PSR_Krueger	1.83	$2.5\ 10^{-3}$	1.18
PSR_ZengL	4.79	$7.8\ 10^{-3}$	0.25
PSR_ZengM	4.45	$2.7\ 10^{-2}$	1.04
PSR_ZengH	5.13	7.02	37.66
PSR_Shen	2.42	$6.2\ 10^{-3}$	13.50
MYR_Hsie	2.30	$1.8\ 10^{-7}$	0.16
MYR_Krueger	1.12	$1.1\ 10^{-3}$	0.71
MYR_ZengL	3.76	$5.2\ 10^{-3}$	0.15
MYR_ZengM	3.55	$1.7\ 10^{-2}$	0.33
MYR_ZengH	4.75	6.32	26.96
MYR_Shen	1.86	$3.3\ 10^{-3}$	7.72
HBR_Hsie	2.39	$2.7\ 10^{-7}$	0.16
HBR_Krueger	1.19	$1.0\ 10^{-3}$	0.75
HBR_ZengL	3.97	$5.4\ 10^{-2}$	0.19
HBR_ZengM	3.52	$1.7\ 10^{-2}$	1.04
HBR_ZengH	5.36	7.20	30.64
HBR_Shen	1.80	$2.0\ 10^{-3}$	7.12

Nearly all simulated mean rain rates are higher than the observed mean rain rates in the four rainfall cases, indicating that the model overestimates the mean rain rate. Shen's scheme produces the closest rain-rate simulations to observations, compared with the other schemes (Fig.2). To explain physical processes responsible for the better rainfall simulations by Shen's scheme, the mean cloud budget [Eq. (1)] is analyzed. Compared to the five other schemes, Shen's scheme generally decreases the rain rate through the hydrometeor change from a strong loss ($Q_{CM}>0$) to a weak gain ($Q_{CM}<0$) in TOGA (Fig.2a) and PSR (Fig.2b) cases and the reduction in hydrometeor loss in MYR (Fig.2c) and HBR (Fig.2d) cases.

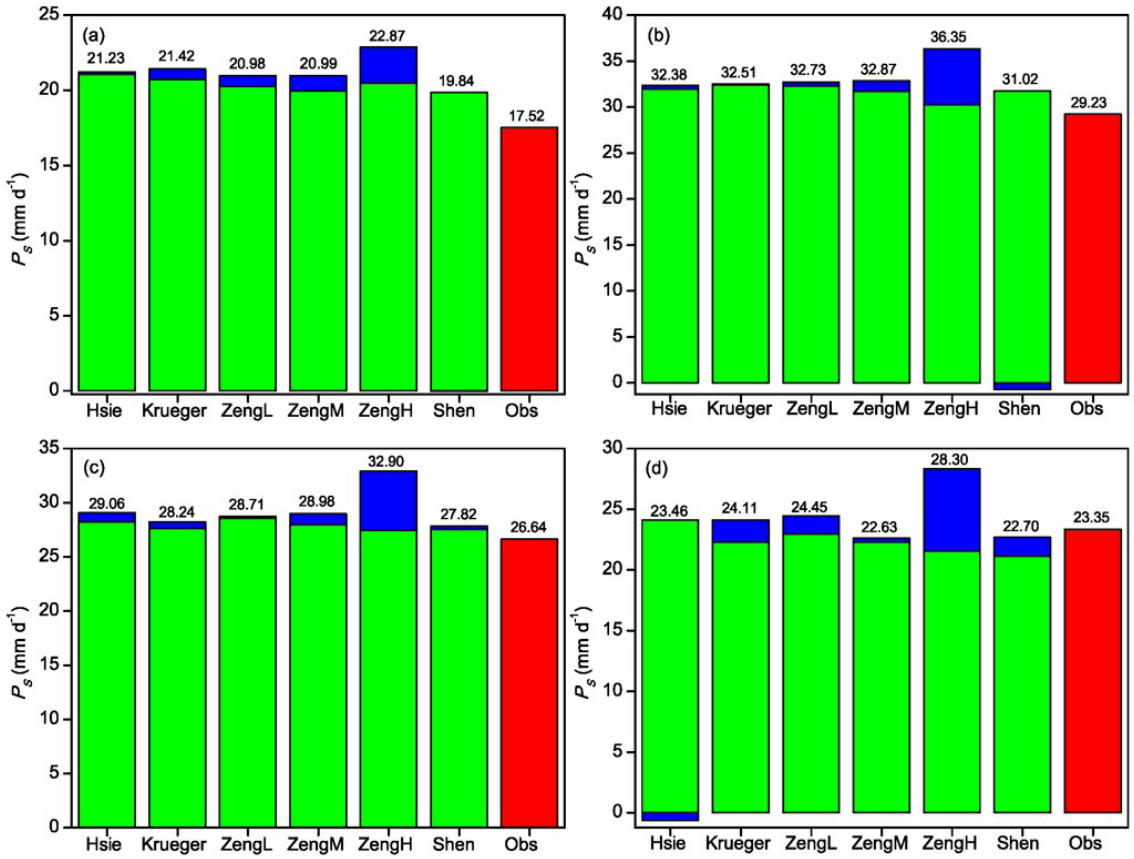

Figure 2. Time-mean simulated rain rate (P_S) from parameterization schemes (Hsie, Krueger, ZengL, ZengM, ZengH and Shen) in (a) TOGA, (b) PSR, (c) MYR and (d) HBR. Observed rain rate is marked by red bar. Simulated rain rate is broken down into net condensation (Q_{NC}; green bar) and hydrometeor change (Q_{CM}; blue bar). Unit is mm·d^{-1}.

Since Zeng's scheme is modified by Shen's Scheme in modeling depositional growth of ice crystal (Shen et al.[8]), the decrease in hydrometeor loss from ZengH to Shen in the four rainfall cases are analyzed based on [Eq.(2)]. Tables 3a–3d reveal that the decrease in hydrometeor loss from ZengH to Shen is primarily associated with the significant reduction in cloud-water loss while the cloud-ice gain decreases from ZengH to Shen. To explain the changes in cloud water and cloud ice, Eq. (3) will be examined.

Since the difference in cloud microphysical processes that are responsible for the decrease in hydrometeor loss from ZengH to Shen are similar in the four rainfall cases, the MYR case is chosen in the following discussions. Table 4a shows that the reduction in cloud water loss from MYR_ZengH to MYR_Shen corresponds primarily to the significant decrease in P_{IDW}. Shen's scheme also suppresses the cloud ice gain through the significant reduction in P_{IDW} although P_{SACI}, P_{SFI} and P_{SAUT} decrease from MYR_ZengH to MYR_Shen (Table 4b).

The reductions in hydrometeor loss from MYR_Krueger and MYR_ZengM to MYR_Shen (Fig. 2c) correspond generally to the enhancement in cloud-water gain from MYR_Krueger to MYR_Shen and the change in cloud water from a loss in MYR_ZengM to a gain in MYR_Shen, as well as the change in cloud ice from a loss in MYR_Krueger to a gain in MYR_Shen and the increase in cloud-ice gain from MYR_ZengM to MYR_Shen (Table 3e). Both increase in cloud-water gain from MYR_Krueger to MYR_Shen and the cloud-water change from a loss in MYR_ZengM to a gain in MYR_Shen are associated with the reductions in P_{RACW} and P_{GACW} (Table 4c). The decrease in P_{GACW} from MYR_Krueger to MYR_Shen corresponds to the reduction in P_{CND}. The heat budgets in MYR_Krueger and MYR_Shen and their difference are analyzed to explain the decreases in P_{RACW} and P_{GACW}. The local change of temperature is associated with condensational heating, convergence of vertical heat flux, temperature advection and radiative heating (also see (2.2) in Gao and Li [34]). The increase in ice hydrometeor mixing ratio (the sum of maxing ratios of five cloud species) from MYR_Krueger to MYR_Shen, which causes the change in infrared radiative tendency from a cooling in MYR_Krueger to a warming in MYR_Shen in the upper troposphere (Fig.3). This leads to the suppressed atmospheric cooling (Fig.3a). The decrease in P_{CND} from MYR_Krueger to MYR_Shen is associated with the increase in saturation specific

humidity as a result of the weakened atmospheric cooling. The decrease in P_{GACW} is also consistent with the suppressed atmospheric cooling. The cloud-ice change from a loss in MYR_Krueger to a gain in MYR_Shen is related to the decrease in conversion from cloud ice to snow (P_{SAUT}) associated with the suppressed atmospheric cooling (Table 4d). The increase in cloud-ice gain from MYR_ZengM to MYR_Shen corresponds to the reduction in P_{SAUT} while the decrease in P_{SFI} is largely balanced by the reduction in P_{DEP}.

Since the time-mean rainfall responses to schemes may be different from time varying responses to schemes, time series of hourly data from six experiments and observation is plotted in Fig.4. Fig.4 shows that the MYR_ZengH gives a higher rain rate than others in the first event (9–13 June), whereas the MYR_Hsie represents the largest rain rate in the third event (16 –20 June). This indicates that short-term rainfall is sensitive to the schemes.

Table 3. Breakdown of Q_{CM} in (a) TOGA_ZengH, TOGA_Shen, TOGA_Shen-TOGA_ZengH, (b) PSR_ZengH, PSR_Shen, PSR_Shen-PSR_ZengH, (c) MYR_ZengH, MYR_Shen, MYR_Shen-MYR_ZengH, and (d) HBR_ZengH, HBR_Shen, HBR_Shen-HBR_ZengH and (e) breakdown of Q_{CM} in MYR_Krueger, MYR_ZengM and MYR_Shen and their differences for MYR_Shen-MYR_Krueger and MYR_Shen-MYR_ZengM. Unit is mm·d^{-1}.

(a)	TOGA_ZengH	TOGA_Shen	TOGA_Shen-TOGA_ZengH
Q_{CM}	2.38	−0.03	−2.41
Q_{CMW}	2.79	0.12	−2.67
Q_{CMR}	0.46	0.13	−0.33
Q_{CMI}	−0.87	−0.44	0.43
Q_{CMS}	0.07	0.00	−0.07
Q_{CMG}	−0.07	0.16	0.23
(b)	PSR_ZengH	PSR_Shen	PSR_Shen-PSR_ZengH
Q_{CM}	6.10	−0.70	−6.80
Q_{CMW}	6.44	−0.01	−6.45
Q_{CMR}	1.57	0.47	−1.10
Q_{CMI}	−1.78	−0.96	0.82
Q_{CMS}	−0.16	0.18	0.34
Q_{CMG}	0.03	−0.38	−0.41
(c)	MYR_ZengH	MYR_Shen	MYR_Shen-MYR_ZengH
Q_{CM}	5.44	0.28	−5.16
Q_{CMW}	5.71	−0.23	−5.94
Q_{CMR}	0.57	0.89	0.32
Q_{CMI}	−0.84	−0.32	0.52
Q_{CMS}	−0.04	−0.05	−0.01
Q_{CMG}	0.04	−0.01	−0.05
(d)	HBR_ZengH	HBR_Shen	HBR_Shen-HBR_ZengH
Q_{CM}	6.76	1.56	−5.20
Q_{CMW}	6.79	−0.45	−7.24
Q_{CMR}	0.04	0.61	0.57
Q_{CMI}	−0.46	−0.11	0.35
Q_{CMS}	−0.22	0.01	0.23
Q_{CMG}	0.61	1.50	0.89

(e)	MYR_Krueger	MYR_ZengM	MYR_Shen	MYR_Shen-MYR_Krueger	MYR_Shen-MYR_ZengM
Q_{CM}	0.60	1.03	0.28	−0.32	−0.75
Q_{CMW}	−0.01	0.12	−0.23	−0.22	−0.35
Q_{CMR}	0.77	0.89	0.89	0.12	0.00
Q_{CMI}	0.02	−0.05	−0.32	−0.34	−0.27
QCMS	−0.02	−0.12	−0.05	−0.03	0.07
Q_{CMG}	−0.11	0.19	−0.01	0.10	−0.20

Table 4. Breakdown of (a) Q_{CMW} and (b) Q_{CMI} in MYR_ZengH and MYR_Shen and their difference for MYR_Shen-MYR_ZengH and breakdown of (c) Q_{CMW} and (d) Q_{CMI} in MYR_Krueger, MYR_ZengM and MYR_Shen and their difference for MYR_Shen-MYR_Krueger and MYR_Shen-MYR_ZengM. Unit is mm·d^{-1}.

(a)	MYR_ZengH	MYR_Shen	MYR_Shen-MYR_ZengH
Q_{CMW}	5.71	−0.23	−5.94
P_{SACW}	1.64	1.71	0.07
P_{RAUT}	0.16	0.26	0.10
P_{RACW}	20.33	17.90	−2.43
P_{GACW}	6.49	7.27	0.78
P_{IDW}	6.32	0.00	−6.32
$-P_{CND}$	−29.37	−27.47	1.90
(b)	MYR_ZengH	MYR_Shen	MYR_Shen-MYR_ZengH
Q_{CMI}	−0.84	−0.32	0.52
P_{SAUT}	4.69	2.33	−2.36
P_{SACI}	1.87	0.21	−1.66
P_{SFI}	4.75	1.86	−2.89
P_{GACI}	1.15	0.13	−1.02
$-P_{IDW}$	−6.32	0.00	6.32
$-P_{DEP}$	−6.92	−4.80	2.12

(c)	MYR_Krueger	MYR_ZengM	MYR_Shen	MYR_Shen-MYR_Krueger	MYR_Shen-MYR_ZengM
Q_{CMW}	−0.01	0.12	−0.23	−0.22	−0.35
P_{SACW}	1.73	1.64	1.71	−0.02	0.07
P_{RAUT}	0.27	0.28	0.26	−0.01	−0.02
P_{RACW}	18.14	18.12	17.90	−0.24	−0.22
P_{GACW}	8.09	7.51	7.27	−0.82	−0.24
P_{IDW}	0.00	0.02	0.00	0.00	−0.02
$-P_{CND}$	−28.30	−27.49	−27.47	0.81	0.02
(d)	MYR_Krueger	MYR_ZengM	MYR_Shen	MYR_Shen-MYR_Krueger	MYR_Shen-MYR_ZengM
Q_{CMI}	0.02	−0.05	−0.32	−0.34	−0.27
P_{SAUT}	3.84	3.09	2.33	−1.51	−0.76
P_{SACI}	0.16	0.03	0.21	0.05	0.18
P_{SFI}	1.12	3.55	1.86	0.74	−1.69
P_{GACI}	0.18	0.06	0.13	−0.05	0.07
$-P_{IDW}$	0.00	−0.02	0.00	0.00	0.02
$-P_{DEP}$	−5.27	−6.75	−4.80	0.47	1.95

To further conduct the quantitative analysis, rain rate, variance and timing of onset and dissipation of rainfall in MYR case are examined in three rainfall events. Following Li and Li [35], 0800 LST 9 June – 0000 LST 13 June, 0000 LST 13 June–1200 LST 16 June and 1200 LST 16 June–0800 LST 20 June are defined as the first, second and third rainfall events (also see Fig.4). The MYR_Krueger gives the closest rain rate to the observed rain rate in the first and third events, whereas the MYR_Shen generates the closest rain rate to the observation in the second event (Table 5). The MYR_Hsie shows the same variance to the observation in the first event, whereas the MYR_ZengL and MYR_Krueger have the closest variances to the observed variances in the second and third events respectively. In the first event, the timing of onset is insensitive to schemes when initial cloud condition is set to be cloud free. The dissipations in MYR_Krueger, MYR_ZengM and MYR_Shen occur 1 hour ahead of observation, but the dissipation in MYR_Hsie appears 1 hour later than the observation. In the second event, the MYR_ZengH has the onset exactly when the observation does. The MYR_ZengL shows the dissipation 1 hour before the observation, whereas the MYR_Krueger and MYR_Shen generate the dissipations 1 hour after the observation. In the third event, the onset in MYR_Shen and dissipation in MYR_ZengH occur at the same time as observations do, but the rainfall in MYR_Shen only lasts for a very short period, pauses and starts again.

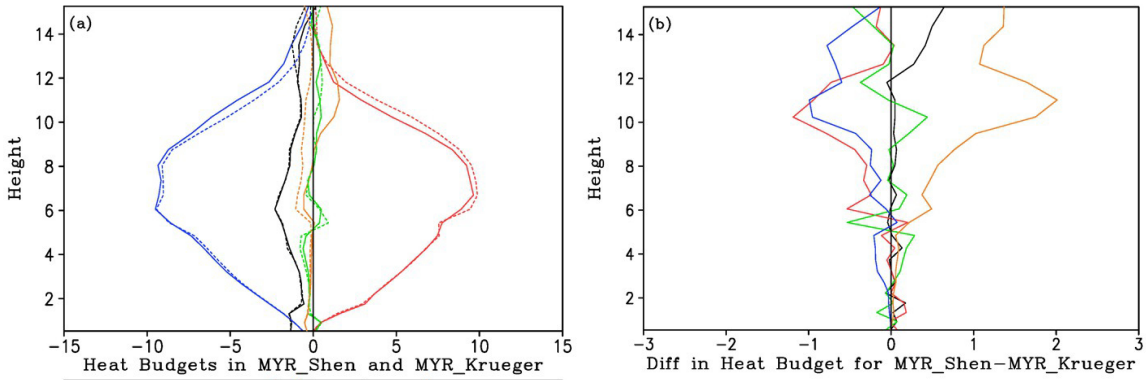

Figure 3. Vertical profiles of (a) local temperature change (black), condensational heating (red), convergence of vertical heat flux (green), temperature advection (blue), and radiation (orange) averaged for 11 days over model domain in MYR_Shen (solid) and MYR_Krueger (dashed) and (b) their differences for MYR_Shen-MYR_Krueger. Unit is ℃ d^{-1}.

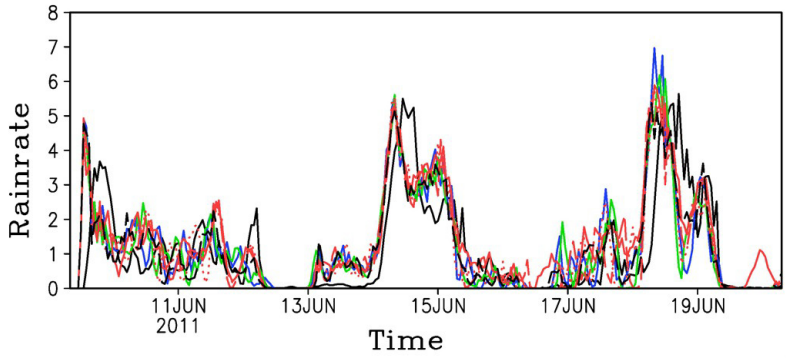

Figure 4. Time series of simulated mean rain rate in MYR_Hsie (cyan solid), MYR_Krueger (green solid), MYR_ZengL (red dot), MYR_ZengM (red dash dot), MYR_ZengH (red solid), MYR_Shen (black dash) and Obs (black solid). Unit is mm·h^{-1}.

Table 5. Mean rain rate (mm h^{-1}), variance ($mm^2 \cdot h^{-2}$) and timing of onset and dissipation of rainfall in MYR case and observation in (a) 0800 LST 9 June–0000 LST 13 June, (b) 0000 LST 13 June–1200 LST 16 June, and (c) 1200 LST 16 June–0800 LST 20 June. 1 the rainfall ends at 0000 LST 17 June and starts at 0300 LST 17 June; 2 the rainfall ends at 0100 LST 17 June starts at 0300 LST 17 June.

(a)	Rain rate	Variance	Timing of onset	Timing of dissipation
MYR_Hsie	0.98	0.86	1200 LST 9 June	1200 LST 12 June
MYR_Krueger	0.97	0.82	1200 LST 9 June	1000 LST 12 June
MYR_ZengL	0.99	0.89	1200 LST 9 June	0900 LST 12 June
MYR_ZengM	1.00	0.89	1200 LST 9 June	1000 LST 12 June
MYR_ZengH	1.03	0.83	1200 LST 9 June	0900 LST 12 June
MYR_Shen	0.92	0.90	1200 LST 9 June	1000 LST 12 June
Observation	0.96	0.86	1300 LST 9 June	1100 LST 12 June
(b)	Rain rate	Variance	Timing of onset	Timing of dissipation
MYR_Hsie	1.39	2.18	0100 LST 13 June	1000 LST 16 June
MYR_Krueger	1.37	2.06	0100 LST 13 June	0800 LST 16 June
MYR_ZengL	1.39	2.25	0200 LST 13 June	0600 LST 16 June
MYR_ZengM	1.41	2.03	0300 LST 13 June	1100 LST 16 June
MYR_ZengH	1.55	2.23	0000 LST 13 June	1600 LST 16 June
MYR_Shen	1.35	2.00	0200 LST 13 June	0800 LST 16 June
Observation	1.23	2.41	0000 LST 13 June	0700 LST 16 June
(c)	Rain rate	Variance	Timing of onset	Timing of dissipation
MYR_Hsie	1.24	2.88	1900 LST 16 June	1100 LST 19 june
MYR_Krueger	1.18	2.58	2000 LST 16 June	1000 LST 19 june
MYR_ZengL	1.19	2.27	1900 LST 16 June	1000 LST 19 June
MYR_ZengM	1.20	2.44	2200 LST 16 June	1000 LST 19 June
MYR_ZengH	1.51	2.35	1200 LST 16 June[1]	1500 LST 19 June
MYR_Shen	1.19	2.18	1500 LST 16 June[2]	1100 LST 19 June
Observation	1.17	2.66	1500 LST 16 June	1500 LST 19 June

4 SUMMARY

Four schemes that parameterize depositional growth of ice crystal are tested in the cloud-resolving mode simulations of four rainfall cases over tropics and midlatitudes in this study. The improvement of rain-rate simulation by Shen's scheme and associated physical process are studied through the comparison between the observations and simulations and the analysis of cloud and heat budgets. The simulations generally show overestimations of rain rate compared to the observations. The scheme developed by Zeng et al.[5] could produce anomalous cloud ice and rainfall when ice nuclei concentration is high. Shen's scheme significantly cuts rain rate and cloud ice and produces the closest rain-rate simulation to the observation through the decrease in hydrometeor loss in response to the dramatic reduction in depositional growth of cloud ice from cloud water. Compared with the other schemes developed by Hsie et al.[1], Krueger et al.[3] and Zeng et al.[5] with low and medium ice nuclei concentration, Shen's scheme also reveals the better rainfall simulation due to it enhances cloud ice and produces the infrared radiative warming in the upper troposphere, which weakens atmospheric cooling. The suppressed atmospheric cooling reduces the hydrometeor loss and thus rainfall through the decreases in collection of cloud water by rain, accretion of cloud water by graupel and conversion from cloud ice to snow.

Although the rainfall events over the tropics and midlatitudes are analyzed in this study, cautions should be exercised for the application of the results from the two-dimensional cloud-resolving model simulations. Therefore, three-dimensional model simulation is required to generalize the results from the two-dimensional model simulations.

Acknowledgement: The authors thank W.-K. Tao at NASA/GSFC for his cloud resolving model and the two anonymous reviewers for their constructive comments.

REFERENCES:

[1] HSIE E Y, FARLEY R D, ORVILLE H D. Numerical simulation of ice-phase convective cloud seeding [J]. J Appl Meteor, 1980, 19(8): 950-977.

[2] FU Q, LIOU K N. Parameterization of the radiative properties of cirrus clouds [J]. J Atoms Sci, 1993, 50(13): 2008-2025.

[3] KRUEGER S K, FU Q, LIOU K N, et al. Improvement of an ice-phase microphysics parameterization for use in numerical simulations of tropical convection [J]. J Appl Meteor, 1995, 34(1): 281-287.

[4] LI X F, SUI C H, LAU K M, et al. Large-scale forcing and cloud-radiation interaction in the tropical deep convective regime [J]. J Atmos Sci, 1999, 56(17): 3028-3042.

[5] ZENG X P, TAO W K, LANG S, et al. On the sensitivity of atmospheric ensembles to cloud microphysics in long-term cloud-resolving model simulations [J]. J Meteor Soc Japan, 2008, 86(5): 45-65.

[6] ZENG X P, TAO W K, ZHANG M H, et al. A contribution by ice nuclei to global warming [J]. Quart J Roy Meteor Soc, 2009, 135(643): 1614-1629.

[7] ZENG X P, TAO W K, ZHANG M H, et al. An indirect effect of ice nuclei on atmospheric radiation [J]. J Atmos Sci, 2009, 66(1): 41-61.

[8] SHEN X Y, HUANG W, QING T, et al. A modified scheme that parameterizes depositional growth of ice crystal: A modeling study of pre-summer torrential rainfall case over southern China [J]. Atmos Res, 2014, 138(3): 293-300.

[9] LIN Y L, FARLEY R D, ORVILLE H D. Bulk parameterization of the snow field in a cloud model [J]. J Climate Appl Meteor, 1983, 22(6): 1065-1092.

[10] SOONG S T, OGURA Y. Response of tradewind cumuli to large-scale processes [J]. J Atmos Sci, 1980, 37(9): 2035-2050.

[11] SOONG S T, TAO W K. Response of deep tropical cumulus clouds to Mesoscale processes [J]. J Atmos Sci, 1980, 37(9): 2016-2034.

[12] TAO W K, SIMPSON J. The Goddard Cumulus Ensemble model. Part I: Model description [J]. Terr Atmos Oceanic Sci, 1993, 4(5): 35-72.

[13] SUI C H, LAU K M, TAO W K, et al. The tropical water and energy cycles in a cumulus ensemble model. Part I: Equilibrium climate [J]. J Atmos Sci, 1994, 51(5): 711-728.

[14] SUI C H, LI X, LAU K M. Radiative-convective processes in simulated diurnal variations of tropical oceanic convection [J]. J Atmos Sci, 1998, 55(13): 2345-2359.

[15] RUTLEDGE S A, HOBBS P V. The mesoscale and microscale structure and organization of clouds and precipitation in midlatitude cyclones. VIII: A model for the "seeder-feeder" process in warm-frontal rainbands [J]. J Atmos Sci, 1983, 40(5): 1185-1206.

[16] RUTLEDGE S A, HOBBS P V. The mesoscale and microscale structure and organization of clouds and precipitation in midlatitude cyclones. XII: A diagnostic modeling study of precipitation development in narrow cold-frontal rainbands [J]. J Atmos Sci, 1984, 41(20): 2949-2972.

[17] TAO W K, SIMPSON J, MCCUMBER M. An ice-water saturation adjustment [J]. Mon Wea Rev, 1989, 117(1): 231-235.

[18] CHOU M D, KRATZ D P, RIDWAY W. Infrared radiation parameterization in numerical climate models [J]. J Climate, 1991, 4(4): 424-437.

[19] CHOU M D, SUAREZ M J, HO C H, et al. Parameterizations for cloud overlapping and shortwave single scattering properties for use in general circulation and cloud ensemble models [J]. J Climate, 1998, 11(2): 202-214.

[20] CHOU M D, SUAREZ M J. An efficient thermal infrared radiation parameterization for use in general circulation model [R]. NASA Tech Memo, 1994, 3 (2): 85. [Available from NASA/Goddard Space Flight Center, Code 913, Greenbelt, MD 20771.]

[21] TAO W K, SOONG S T. A study of the response of deep tropical clouds to mesoscale processes: Three-dimensional numerical experiments [J]. J Atmos

Sci, 1986, 43(22): 2653-2676.
[22] TAO W K, SIMPSON J, SOONG S T. Statistical properties of a cloud ensemble: A numerical study [J]. J Atmos Sci, 1987, 44(21): 3175-3187.
[23] GRABOWSKI W W, WU X Q, MONCRIEFF M W, et al. Cloud-resolving model of tropical cloud systems during Phase III of GATE. Part II: Effects of resolution and the third spatial dimension [J]. J Atmos Sci, 1998, 55 (21): 3264-3282.
[24] TOMPKINS A M. The impact of dimensionality on long-term cloud-resolving model simulations [J]. Mon Wea Rev, 2000, 128(5): 1521-1535.
[25] KHAIROUTDINOV M F, RANDALL D A. Cloud resolving modeling of the ARM summer 1997 IOP: Model formulation, results, uncertainties, and sensitivities [J]. J Atmos Sci, 2003, 60(4): 607-625.
[26] SUI C H, LI X F, YANG M J, et al. Estimation of oceanic precipitation efficiency in cloud models [J]. J Atmos Sci, 2005, 62(12): 4358-4370.
[27] WANG Y, SHEN X Y, LI X F. Microphysical and radiative effects of ice clouds on responses of rainfall to the large-scale forcing during pre-summer heavy rainfall over southern China [J]. Atmos Res, 2010, 97(1): 35-46.
[28] SHEN X Y, WANG Y, LI X F. Effects of vertical wind shear and cloud radiative processes on responses of rainfall to the large-scale forcing during pre-summer heavy rainfall over southern China [J]. Quart J Roy Meteor Soc, 2011, 137(654): 236-249.
[29] ZHAI Guo-qing, LI Xiao-fan, ZHU Pei-jun, et al. Surface rainfall and cloud budgets associated with Mei-yu torrential rainfall over eastern China during June 2011 [J]. Adv Atmos Sci, 2014, 31(6): 1435-1444.
[30] SHORT D A, KUCERA P A, FERRIER B S, et al. Shipboard radar rainfall patterns within the TOGA/COARE IFA [J]. Bull Amer Meteor Soc, 1997, 78(12): 2817-2836.
[31] JOYCE R J, JANOWIAK J E, ARKIN P A, et al. CMORPH: A method that produces global precipitation estimates from passive microwave and infrared data at high spatial and temporal resolution [J]. J Hydrometeor, 2004, 5(3): 487-503.
[32] ZENG X P, TAO W K, MATSUI T, et al. Estimating the ice crystal enhancement factor in the tropics [J]. J Atmos Sci, 2011, 68(7): 1424-1434.
[33] FLETCHER N H. The Physics of Rainclouds [M]. Cambridge: Cambridge University Press, 2011: 241.
[34] GAO S T, LI X F. Cloud-Resolving Modeling of Convective Processes [M]. Dordrecht: Springer, 2008: 206.
[35] LI Ting-ting, LI Xiao-fan. Barotropic processes associated with the development of Meiyu precipitation system [J]. Adv Atmos Sci, 2016, 33(5): 593-598.
[36] KOENIG L R. Numerical modeling of ice deposition [J]. J Atmos Sci, 1971, 28(2): 226-237.
[37] HALLETT J, MOSSOP S C. Production of secondary ice particles during the riming process [J]. Nature, 1974, 249 (5452): 26-28.

Citation: XIN Jin and LI Xiao-fan. A modeling study of parameterization schemes for depositional growth of ice crystal: four rainfall cases over tropics and midlatitudes [J]. J Trop Meteor, 2017, 23(3): 259-268.